Journal of Computers Vol. 29 No. 2, 2018, pp. 193-204
doi:10.3966/199115992018042902019

Thermal Infrared Radiation Calculation of Orbital Objects with Micro-motions

Fu-bing Li[1*], Jun-min Leng[1], Lin Cao[1], Xiao-jian Xu[2]

[1] School of Information & Communication Engineering, Beijing Information Science & Technology University, Beijing 100101, ROC
{lifubing, lengjunmin, charlin}@bistu.edu.cn

[2] School of Electronics and Information Engineering, Beihang University, Beijing 100191, ROC
xiaojianxu@buaa.edu.cn

Received 24 July 2017; Revised 19 September 2017; Accepted 19 October 2017

Abstract. Effect of micro-motion dynamics on infrared (IR) radiation signatures for orbital objects is studied in this work, by considering the micro-motion modes and physical principles based heat transfer. Micro-motion modes of an object on orbit such as spin stabilization, three-axis stabilization or roll motion are modeled using Rodrigues formulation. Heat transfer equations, including three-dimensional (3-D) heat conduction, radiation on outer surface including thermal dissipation as well as heating from the sun and earth, and thermal radiation on innermost surface, are formulated and solved using numerical techniques to obtain the time-evolving temperature field on the object. IR signatures in 8~16μm bands are calculated by integrating the self-emitted and surface-reflected components, with different surface emissivity being considered. Numerical results of the micro-motion effect on IR signatures for a cylindrical object on orbit are presented with in-depth phenomenological analysis.

Keywords: heat transfer, IR radiation, micro-motion, modeling, orbital object

1 Introduction

The temperature of a orbital object tends to be time-evolving due to the heat loss, surface heating from the Sun and Earth in space [1]. Viewed from a spaceborne sensor, IR radiation of the object mainly contains three components, namely self-emitted energy, surface-reflected energy from the Sun and Earth. Self-emitted energy depends on temperature and surface emitting properties, while the surface-reflected radiation relates with the Solar/Earth irradiation and surface reflecting properties (i.e., bidirectional reflectance distribution function, BRDF) of the object [2-3].

Temperature and infrared characteristics of space objects have been studied in many papers. Han et al. presented an infrared model of satellite for distinguishing the working and no-working satellite [1]. Zuo et al. analyzed the rigid-flexible-thermal coupling of satellite solar-panels in low earth orbit [4]. Wang et al. established an infrared model of the on-orbit target to detect the satellite using material properties [5]. Wu studied the influence of the multilayer heat insulation materials on satellite temperature as well as infrared signature [6]. Lu et al. calculated the effect of solar absorption coefficient on temperature of a three-axis stabilization satellite [7]. Shen et al. simulated the optical properties of sun-synchronous orbit satellite and then verified the result using experimental data [8]. Yang et al. modeled the periodical temperature as well as the infrared radiation of an orbital satellite [9]. Generally, a 2-D network might be enough for thin-walled objects or objects with spinning motion [10], but a 3-D heat transfer network is required to deal with objects with thick-walls [11].

Spinning and three-axis stabilization are two common ways to stabilize orbital objects such as satellites. When the object is out of control, it might undergo roll motion. Surface heating can be easily

* Corresponding Author

calculated when the object keeps still. However, it will be complicated if the object undergoes micro-motion dynamics such as spinning or rolling. These motions, namely micro-motions, can affect not only the temperature distribution, but also the IR radiation characteristics of an orbital object [12]. Zhu et al. performed an experiment to study factors of influencing the temperature of a space object, including surface heating and spinning, et al [13]. Mao et al. studied the influence of spin and roll motion on balloons in space [14]. Liu et al. estimated the parameters of micro-motion dynamics and geometrical shape of exoatmospheric infrared targets [15]. Studies above reveal that the temperature as well as infrared characteristics of space objects differs a lot under different motions.

In this paper, a complete procedure is developed to calculate the temperature and IR radiation characteristics for orbital objects. Using the procedure, the IR characteristics of a cylindrical object on orbit with different surface emissivity and stabilization modes are calculated and phenomenologically analyzed. The remainder of the context is organized as follows. Dynamics model for space objects is established and aspect transform matrices are derived in Section 2. Physical principles based heat transfer is discussed, and the unsteady-state temperature as well as the IR radiation is calculated in Section 3. Time-evolving surface temperature and thermal IR radiation for a cylinder object with different emissivities and stabilization modes are studied with detailed phenomenological analysis in Section 4. Conclusion is provided in Section 5.

2 Dynamics Model for Orbital Objects

2.1 3-D Rotation of a Rigid Body

Spin stabilization, three-axis stabilization and roll-motion can all be seen as rigid body dynamics, which has been described in detail previously [16]. Consequently, motions involved for orbital objects will be described in brief.

Fig. 1 illustrates a moving object in geocentric inertial coordinate system (U, V, W). The angular velocity vector $\vec{\omega}$ =[ω_x, ω_y, ω_z]^T is defined in local coordinates (x, y, z) attached to the object itself. A reference coordinate system (X, Y, Z), which parallels to the system (U, V, W) and shares the same origin with the system (x, y, z), is also introduced to simplify the analysis required for the rotating object.

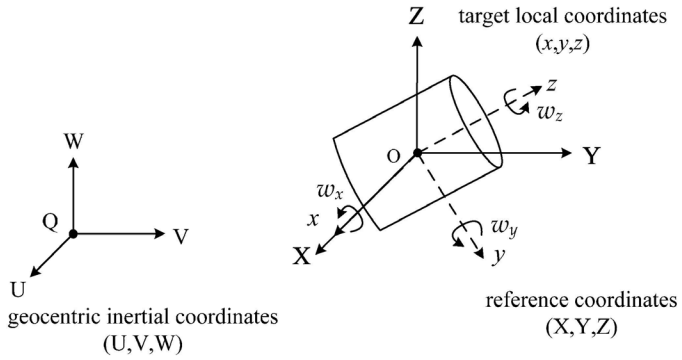

Fig. 1. A rotating object in geocentric inertial coordinate system

Viewed from the reference coordinate system (X, Y, Z), the unit vector of the rotation for the object is

$$\vec{\omega}' = [\omega_x', \omega_y', \omega_z']^T = R_{Init} \frac{\vec{\omega}}{\| \vec{\omega} \|}. \quad \textbf{(1)}$$

where $\Omega = \| \vec{\omega} \|$ is the vector module and R_{Init} is the initial orientation matrix of the object. According to the Rodrigues formula [16], the rotation matrix as a function of time t can be expressed as

$$R_t = I + \hat{\omega}' \sin \Omega t + \hat{\omega}'^2 (1 - \cos \Omega t). \quad \textbf{(2)}$$

where I is the identity matrix, and $\hat{\omega}'$ is a skew symmetric matrix

$$\hat{\omega}' = \begin{bmatrix} 0 & -\omega_z' & \omega_y' \\ \omega_z' & 0 & -\omega_x' \\ -\omega_y' & \omega_x' & 0 \end{bmatrix}. \quad \textbf{(3)}$$

Thus, an initial position $\boldsymbol{r}_0=[x_0, y_0, z_0]^T$ in local coordinate system (x, y, z) will be $R_{Init}\,\boldsymbol{r}_0$ in the reference coordinate system. At time t, the corresponding position moves to $\boldsymbol{r}_t=R_tR_{Init}\boldsymbol{r}_0$.

2.2 Rotation Matrices of Spin, Three-axis Stabilization and Roll Motion

As shown in Fig. 2(a), consider an object rotates with a scalar angular velocity ω_s around its z-axis in local coordinate system, the corresponding angular velocity vector $\vec{\omega}$ is $[0, 0, \omega_s]^T$. Substitute the vector $\vec{\omega}$ into Eqs. (1)-(3), we will get the spinning rotation matrix, R_{st}, in reference coordinate system.

In this article, the three-axis stabilization will be simplified as the object keeps still in in reference coordinates (X, Y, Z), as depicted in Fig. 2(b). As a result, the rotation matrix for the three-axis stabilization will not change as a function of time, and can be written as $R_{3t}= R_{Init}$, where the R_{Init} is the initial orientation matrix of the object.

As illustrated in Fig. 2(c), the roll motion in this article is defined as the object's rotation around its y-axis. Assume the object rolls with a scalar angular velocity $\omega_r=2\pi/T_r$, where T_r is the rolling period, the corresponding angular velocity vector $\vec{\omega}$ can be written as $[0, \omega_r, 0]^T$. Thus the rolling rotation matrix R_{rt} can be obtained by substituting the vector $\vec{\omega}$ into Eqs. (1)-(3).

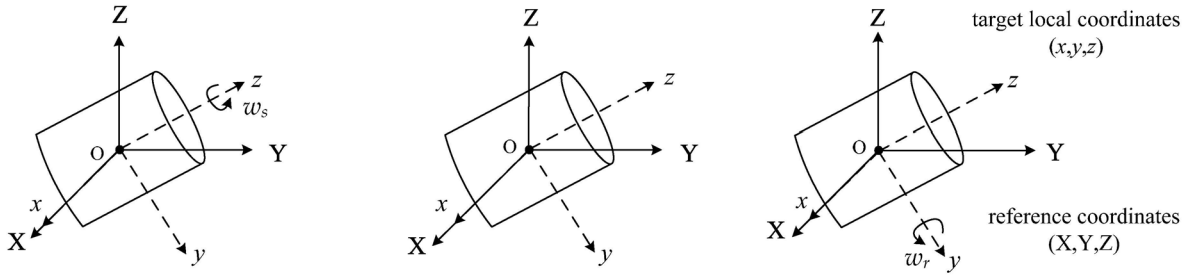

(a) spinning (b) 3-axis stabilization (c) rolling motion

Fig. 2. A spinning, three-axis stabilization, and rolling object in reference coordinate system

3 Temperature and Infrared Radiation Calculation

Without loss of generality, we analyze the heat transfers of a cylindrical object on orbit. Given a cylinder radius, height, and thickness of material, the object is built, as shown in Fig. 3(a). Then the object is decomposed into volume elements in cylindrical coordinates for the preparation of heat transfer calculation. The difference equation of energy conservation for p-th volume element is

$$\rho c \frac{T_p(t+\Delta t)\text{-}T_p(t)}{\Delta t} dv = W_c(t+\Delta t) + W_{out}(t+\Delta t) + W_{in}(t+\Delta t) + qdv. \quad \textbf{(4)}$$

where ρ, c, and dv are density, specific heat of material, and differential volume, respectively. T denotes temperature in kelvins, and Δt is time increment step. W_c, W_{out} and W_{in} are net incoming heat flow of the conduction heat transfer, surface heating and radiative heat transfer on inner-surface, respectively. q is the volume heat source term. The left side of the Eq. (4) stands for the increased internal energy, while the right side is the energy flows into a volume element. Note that W_{out} and W_{in} are zeros if an element is surrounded by other elements. Temperature variation of the element can be solved by using numerical methods [17-18].

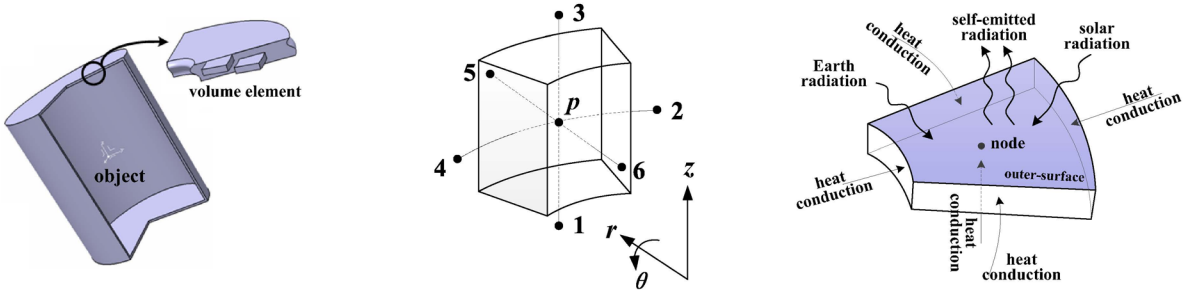

(a) Geometry of the object (b) surrounding nodes of node *p* (c) heat transfer of an element

Fig. 3. Geometry and volume elements of a cylindrical object

3.1 Conduction Heat Transfer

As depicted in Fig. 3(b), heat conduction from the six surrounding elements can be written as

$$W_c(t) = \sum_{i=1}^{6} k_i \frac{S_i}{d_i}(T_i(t) - T_p(t)). \tag{5}$$

where k_i is the thermal conductivity for i-th element, S_i is the contact area of two neighboring elements, and d_i is the conduction distance between two elements, respectively. Note that the surrounding nodes can be less than six if the element happens to be on the outermost or innermost surface.

3.2 Surface Heat Transfer

As shown in Fig. 3(c), heat transfer on outer-surface mainly contains three parts: thermal dissipation into the space (W_d), surface heating from the Sun (W_s) and the Earth (W_e), which yields

$$W_{out}(t) = W_s(t) + W_e(t) - W_d(t). \tag{6}$$

As the orbital object moves continuously around the Earth, the judgment of the object in or out of the Earth's shadow is required head of Eq. (6). Furthermore, as the object undergoes micro-motions continuously, it is possible that a surface element receives the solar radiation at this moment and can't receive solar energy at that moment. Thus a factor, η_s, is introduced to quantify the solar illumination on each surface element during one heat transfer step $[t, t+\Delta t)$, which can be easily calculated by averaging the cosine of the angle between the solar vector and surface norm [12]. In this way, the solar energy absorbed by a surface element is written as

$$W_s(t) = E_0 \eta_s(t) \alpha_s S_o. \tag{7}$$

where E_0 is the solar constant, 1367W/m^2, α_s is the solar energy absorption coefficient, S_o is the surface area.

For simplicity, the Earth is considered as a greybody with equilibrium temperature T_e and emissivity ε_e. Thus the energy absorbed by a surface element can be express as

$$W_e(t) = \left(\varepsilon_o \varepsilon_e \sigma T_e^4 \left(R_e / r_{obj} \right)^2 + \alpha_s E_{rs} \right) \eta_e(t) S_o. \tag{8}$$

where σ is Steven-Boltzmann constant, ε_o is the emissivity of the surface element, R_e denotes the Earth radius and r_{obj} represents the distance between the object and the Earth center. E_{rs} is the solar flux reflected from the Earth (known as the albedo flux and typically taken to be equal to $0.3E_0$), and η_e is the average illumination coefficient of the Earth during one heat transfer step.

The self-emitted heat loss of the surface element is governed by the Stefan-Boltzmann's law

$$W_d(t) = \sigma T_o^4(t) \varepsilon_o S_o. \tag{9}$$

where T_o is the temperature of the surface element.

3.3 Radiative Heat Transfer

The surface of the enclosure is assumed to be diffuse-gray. Based on the assumptions, radiative exchange between any two surface elements can be calculated using the view factors. As shown in Fig. 4, the surface radiosity J for element i consists of two parts: the self-emitted heat flux and the reflected incoming irradiation [17]

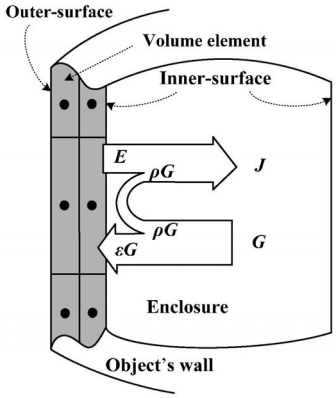

Fig. 4. Radiative heat transfer of the enclosure

$$J_i(t) = \varepsilon_i \sigma T_i^4(t) + \rho_i G_i(t). \tag{10}$$

where ε_i is surface emissivity, ρ_i is reflectivity, and G_i is the irradiation on surface i.

Surface irradiation G_i can be obtained by adding up the energy which leaves surface j and is intercepted by surface i

$$G_i(t) = \frac{1}{s_i}\sum_{j=1}^{N} F_{j-i} J_j(t) s_j = \sum_{j=1}^{N} F_{i-j} J_j(t). \tag{11}$$

where s_i is the surface area of the i-th element. Note that the law of reciprocity is applied in derivation procedure.

The net radiative heat absorption for surface i is written as

$$Q_i(t) = \varepsilon_i \left(G_i(t) - \sigma T_i^4(t) \right) s_i. \tag{12}$$

Let's suppose that the temperature T and view factor F is prescribed. Then the surface radiosity J for each surface in Eq. (10) could be solved by using Gauss-Seidual iteration method, and net radiative heat absorption Q_i in Eq. (12) (corresponding to W_{in} in Eq. (4)) would be calculated consequently.

3.5 Thermal Infrared Radiation

IR radiation from a space object involves self-emitted energy, reflected energy from the sun, earth, and background energy such as stars, et al. In this article, only the first three components are considered in this article. Thus, viewed from a spaceborne IR sensor, surface radiance within a waveband from λ_1 to λ_2 for element i can be calculated as

$$L_i(t) = \int_{\lambda_1}^{\lambda_2} \left(L_o(\lambda, t) + L_s(\lambda, t) + L_e(\lambda, t) \right) d\lambda. \tag{13}$$

where $L_o(\lambda, t)$ is the self-emitted spectral radiance, which can be calculated from the Planck equation. $L_s(\lambda, t)$ and $L_e(\lambda, t)$ are the spectral radiance reflected from the Sun, and Earth, respectively. Both of them can be obtained by multiplying the bidirectional reflectance distribution function of the surface with the corresponding spectral irradiance of the Sun or Earth.

The radiant intensity of the object I_{obj} can be obtained by summing up the contributions of surfaces facing the sensor

$$I_{obj}(t) = \sum_i L_i(t)\Delta s_i(t). \tag{14}$$

where Δs_i is the projected area of the surface i seen by the sensor, which can be obtained by Z-buffer algorithm.

4 Numerical Results and Analysis

To demonstrate, the time-evolving temperature as well as IR signatures for a cylindrical object with different motions and surface emissivities on a near-earth orbit is studied. As shown in Fig. 8, the geocentric inertial coordinate system is defined to describe the object's space position, whose U-axis points to the vernal equinox, W-axis runs along the earth's rotational axis pointing to the North, and V-axis satisfies right-handed coordinate system. The orbit used here is an ideal sun-synchronous orbit, which is modeled by two-body orbit motion formula based on the six orbital elements [19]: semimajor axis a=7077.37km, eccentricity e=0, inclination i=98.183°, right ascension of ascending node Ω=0°, argument of perigee ω=0° and time past perigee t_p=0s. The orbit period is then calculated to be T_p = 5925s.

For simplicity, a long wave (LWIR) 8~16μm band sensor is assumed to locate along the plus X-axis in reference coordinate system (just ahead of the object) and runs together with the object. The solar incidence angle in zenith and azimuth direction is 90° and 0°, respectively, pointing to the minus U-axis. The Earth temperature is assumed to be 290K.

The cylindrical object, with 50cm in radius and 120cm in height, consists of only one material layer, which is supposed to be 1.6cm thick aluminum, as illustrated in Fig. 3(a). The outer-surface emissivity ε is set to be equal to solar absorptivity α_s, which is respectively assumed to be 0.9, 0.5 and 0.1. The initial orientation of the object is shown in Fig. 8, which can be obtained by rotating the local coordinate system (x, y, z) clockwise around its x-axis by 81.817° in reference coordinate. In the current case, the z-axis of the local coordinate system (x, y, z) will be perpendicular to the orbital plane.

Spin stabilization, three-axis stabilization as well as rolling are respectively introduced to calculate the temperature distribution and study the impact of micro-motion on IR signatures of orbital objects. With spin stabilization, the spinning frequency is 1Hz, rotating around its x-axis. For roll motion, the corresponding period is assumed to be 50s, rotating around its y-axis. Initial temperature field of the object is set to be 300K.

As can be seen in Fig. 5, at t=0s, the object starts from location P_1. Surface temperature of the object gradually rises due to the solar radiation. However, when the object enters into the Earth's shadow, surface temperature tends to decrease until it moves out of the shadow again. Fig. 6 illustrates the surface temperature at P_n (the intersection point of x-axis with outer-surface) as a function of time for the spinning object with surface emissivity ε=0.9. Apparently, after dozens of orbital circles, it gradually achieves dynamic equilibrium and finally demonstrates a periodical variation. Note that the remaining results presented below are obtained when the object is in dynamic equilibrium.

4.1 Surface Temperature of the Object with Different Stabilization Modes

Suppose the surface emissivity is 0.9. As illustrated in Fig. 7, surface temperature at P_n demonstrates obvious periodicity in all the three cases (i.e., spinning stabilization, three-axis stabilization and roll motion). During one period [0, 5925s), the object firstly runs in sunshine space before t=1906s, then enters into earth's shadow from t=1906s to 4018s, and moves into the sunshine space again for the remaining time. Surface temperature at P_n apparently demonstrates an increasing-decreasing-increasing process for all the three cases.

Result also indicates that temperature at P_n is obviously higher for the object with three-axis stabilization, compared with the other two cases. It's because that for three-axis stabilization case, P_n is always facing the sun in sunshine space, making its temperature keep rising in sunshine space. With spin stabilization, as the object is rotating around its z-axis in the current case, the outer-surface is illuminated uniformly along the circumference, making the corresponding temperature lower than the three-axis stabilization case. For the roll motion, it is similar to the spinning case. It can be imagined that the temperature of the surface that facing back to the Sun for object with three-axis stabilization will be lower than that with spinning or roll motion.

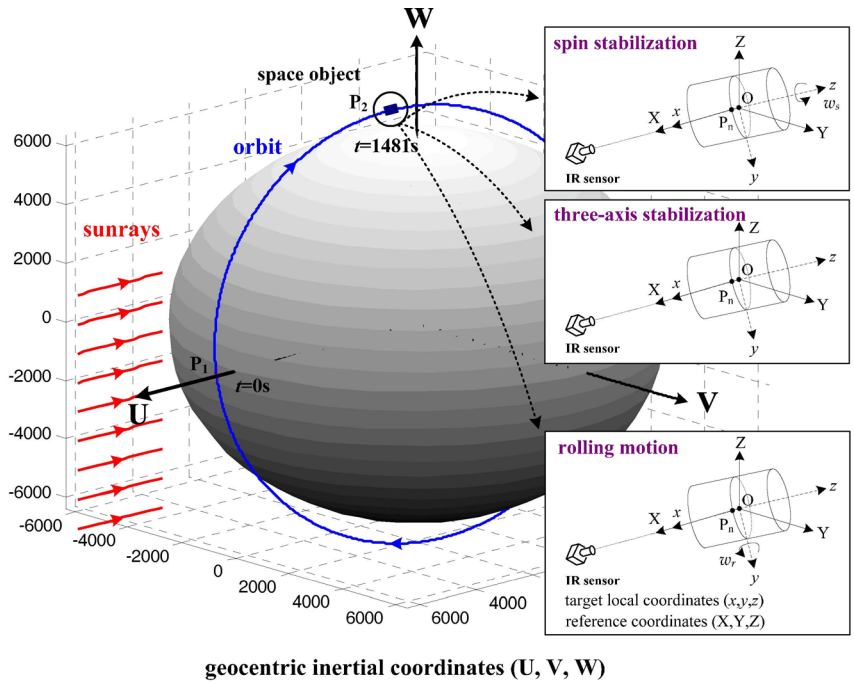

Fig. 5. Simulation scene in geocentric inertial coordinate system

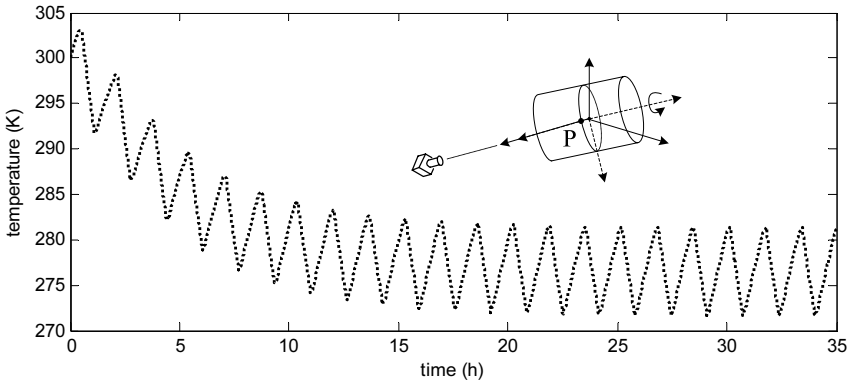

Fig. 6. The process of surface temperature achieving stable, spin stabilization

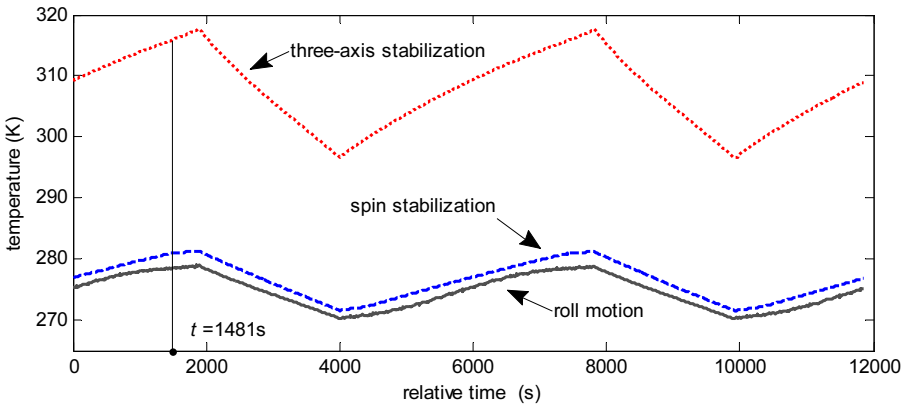

Fig. 7. Surface temperature as a function of time at P_n

Fig. 8 illustrates surface temperature distribution of the object in three cases at t=1481s, corresponding to the orbital position P_2 in Fig. 5. For the object with spinning motion (rotating around its z-axis), as the IR sensor is assumed to locate in the positive X-axis, the projected area of the object viewed from the sensor does not change as a function of time. The projected area of the object with spinning motion is just the same to the three-stabilization. However, the projected area viewed from the IR sensor keeps changing for the rolling object with y-axis as its rotation axis, thus producing a different projection area compared with the other two cases, as depicted in Figs. 8(a)-(c).

As shown in Fig. 8(b), as the object with three-axis stabilization keeps still in reference coordinate system, surface temperature is apparently higher than the other two cases. As illustrated in Fig. 8(a), the temperature difference is tiny along the circumference due to the spinning motion. In addition, with roll motion, although the surface temperature difference is not quite apparent, it also demonstrates some variation along the circumferential direction, as shown in Fig. 8(c).

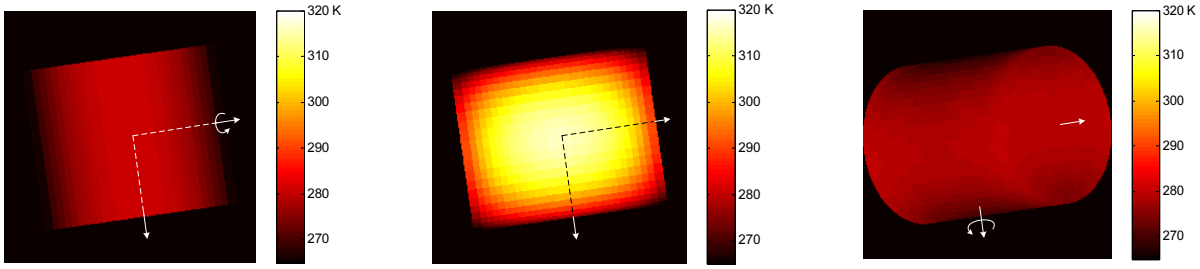

(a) spin stabilization (b) three-axis stabilization (c) roll motion

Fig. 8. Surface temperature distribution at t=1481s

4.2 Radiant Intensity of the Object with Different Stabilization Modes

Fig. 9 illustrates the radiant intensity incident into the IR sensor from the orbital object with three stabilization modes. It can be seen that although the radiant intensity of the object with roll motion undergoes fast fluctuations, however, all the three cases demonstrate apparent periodical variation, where the period is just the same as the orbit period. From the figure, it can be seen that, first, the IR radiant intensity of the spin stabilization, as well as the three-axis stabilization case, shows a similarity to its temperature frame illustrated in Fig. 7. In fact, the mean value of the rolling case also shows the same tendency to its temperature variation. The reason why the radiant intensity of the object with three motions is so different in Fig. 9 can partially be explained in Fig. 10.

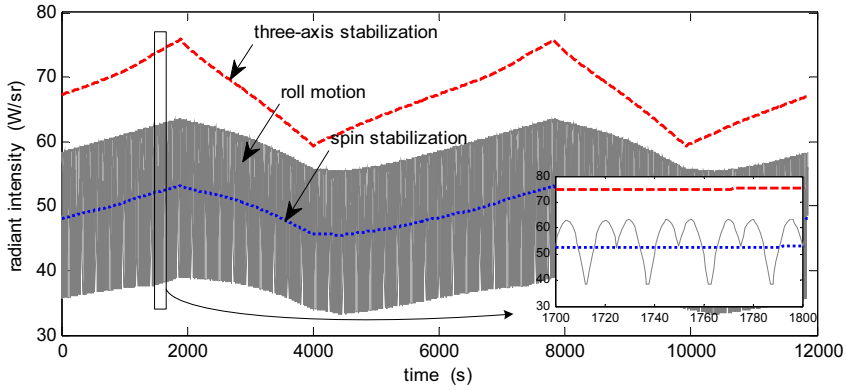

Fig. 9. Radiant intensity of the object with different types of motion in band 8-16μm

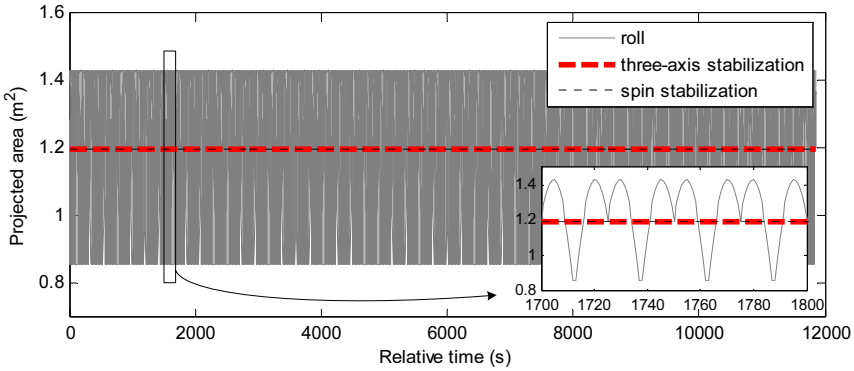

Fig. 10. Projected area of the object with different types of motion

As illustrated in Fig. 10, for the current observing geometry, the projected area to the sensor is always 1.2m^2 when the object undergoes spin stabilization or three-axis stabilization on orbit. According to Wien displacement law, the max radiant wavelength of the surface temperature in Fig. 7 is just among the sensor's band, 8~16 μm. As a result, the radiant intensity is mainly determined by the self-emitted energy when the emissivity is high. In this case, the surface temperature is 0.9. Thus the radiant intensity of the object with spinning or three-axis stabilization shows a similar tendency with their temperature curves.

Second, with roll motion, the corresponding radiant intensity demonstrates double time-scale variation. The larger scale corresponds to the orbital period, while the smaller scale is coincident with the micro-period of the roll motion. In fact, it is the fluctuation of the projected area that results in the violent variation of the IR signature. As depicted in Fig. 8(c), viewed from the IR sensor, the projected area of the object will change periodically when it rotates around it *y*-axis. The fluctuation of the projected area within several rolling periods is shown in the zoom-in area in Fig. 10.

4.3 Thermal Infrared Characteristics with Different Emissivities

As can be seen from Section 4.1 and 4.2, the radiant intensity of the object is mainly determined by both the temperature and the projected area when the surface emissivity of the object is relatively high. However, it is not always the case, especially when surface emissivity is low.

Take spin stabilization for example. Fig. 11 illustrates temperature variations as a function of time at the specified point P_n on object when surface emissivity is 0.9, 0.5 and 0.1, respectively. From Fig. 11, a conclusion can be drawn that higher emissivity produces higher temperature fluctuation, which can be explained from the fact that object with higher emissivity can absorb more solar/Earth radiation, thus producing a higher temperature during the same time period. When the surface emissivity is 0.9, the temperature difference over a period is as high as 10K in the current case. On the other hand, it is less than 2K when the emissivity is 0.1. At this time, the periodicity can barely be seen. Furthermore, the average temperature tends to descend as the surface emissivity gets lower.

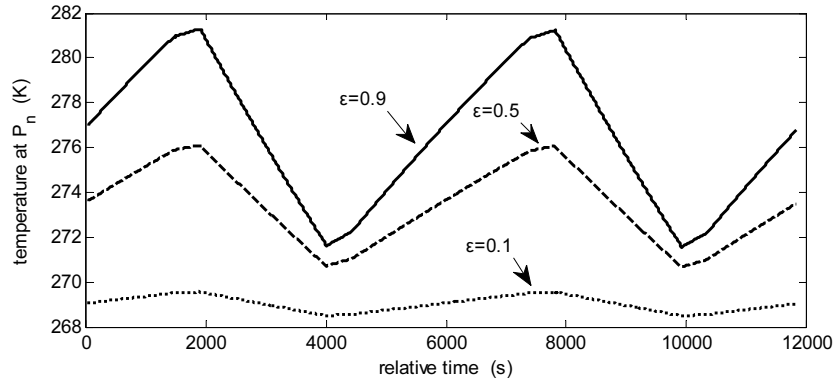

Fig. 11. Surface temperature at P_n, with different emissivity, spin stabilization

Fig. 12 illustrates the radiant intensity of the spinning object when the surface emissivity is 0.9, 0.5 and 0.1, respectively. The energy components of the radiant intensity, namely the self-emitted energy, reflected energy from the Sun and the Earth, are also depicted in Fig. 16 for the object with different surface emissivities.

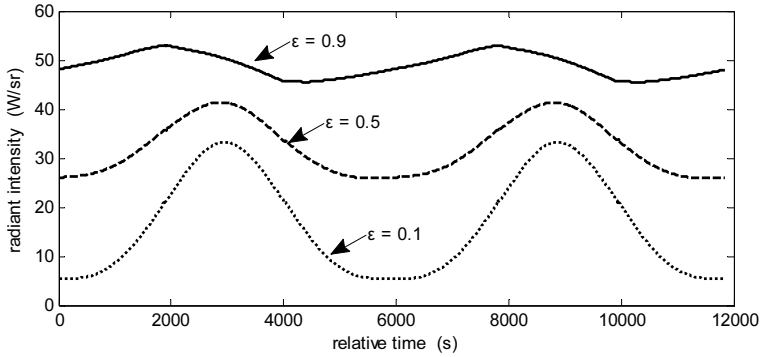

Fig. 12. Radiant intensity with different emissivity, 8~16μm, spin stabilization

From Fig. 12, for long wave IR band, it can be also been seen that as surface emissivity decreases, the corresponding average radiant intensity decreases, too. This can be explained as follows. As the emissivity decreases, the temperature decreases too, and this can be evidenced by Fig. 11. Thus the self-emitted energy of the surface will decreased correspondingly. In such cases, although the increased reflectivity leads to an increase in surface reflection, as shown in Fig. 13(a) through (c), however, the decreased amount of the self-emitted energy is more than the increased surface energy. As a result, the average radiant intensity of the object decreases along with the surface emissivity. In addition, although the self-emitted component dominates the total energy in long wave band when the surface emissivity is close to 1, as shown in Fig. 13(a), however, surface-reflected energy from the earth becomes dominant with low emissivity, as can be seen in Fig. 13(c).

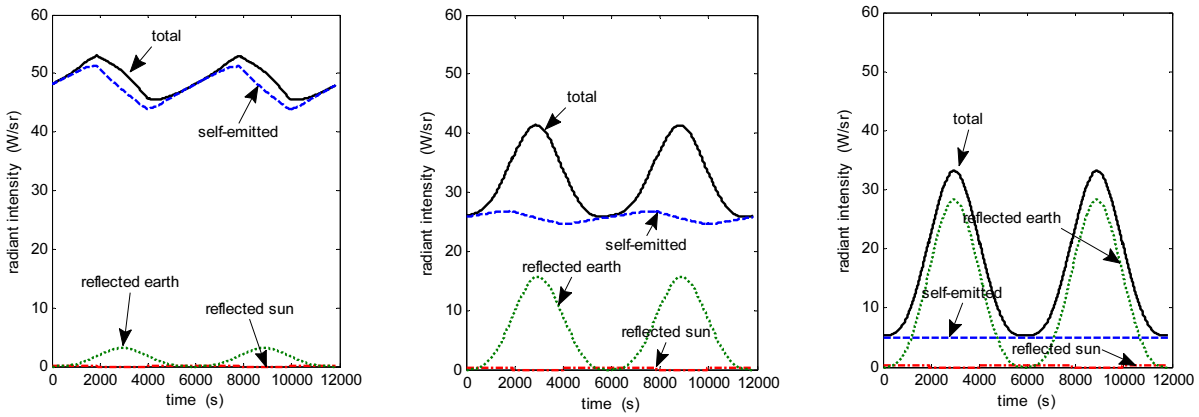

(a) $\varepsilon = 0.9$ (b) $\varepsilon = 0.5$ (c) $\varepsilon = 0.1$

Fig. 13. Radiant components of the object with different emissivity, 8~16μm, spin stabilization

5 Concluding remarks

In this work, the periodical temperature and thermal IR signatures of a near-earth orbital object with different motions are calculated and studied, considering the heat-transfer, stabilization mode as well as specified observation geometry. The impact of surface emissivity on temperatures and IR signatures is also analyzed. Numerical results indicate that: (1) For all the three cases, i.e., spin stabilization, three-axis stabilization or roll motion, the object demonstrates periodical characteristics on temperature and IR signatures. However, different stabilization modes result in different steady-state variation of surface temperatures; and (2) In long wave IR band, the higher the surface emissivity is, the larger the fluctuation

of the surface temperature and total IR radiant intensity are. As a consequence, in order to keep the temperature constant on orbit, materials with small emissivity need to be used.

Note that all the numerical results in this paper are physics based and under the assumptions that the earth is a greybody with constant temperature. As a consequence, the corresponding irradiation on the orbital object from the earth is approximated. In order to get more accurate results, the irradiation above the atmosphere is time-and-space dependent because of the combined impact from the temperature distribution of the earth's surface, the atmospheric effect and so on. This will be further studied in the future.

Acknowledgements

This work was supported by Beijing Natural Science Foundation (No. 3164043), National Natural Science Foundation of China (No. 61671069) and Science and Technology Projects of Beijing Municipal Education Commission (No. KM201411232009).

References

[1] Y.G. Han, Y.M. Xuan, Infrared feature of the satellite, Infrared and Laser Engineering 34(1)(2005) 34-37.

[2] J.H. Choi, T.K. Kim, Characteristic analysis of IR signatures for different optical surface properties by computer modeling and field measurement, in: Proc. SPIE 7830, 2010.

[3] F. Yang, Y.M. Xuan, Y.G. Han, Infrared characteristics of spacecraft undulating surface, Infrared and Laser Engineering 45(5)(2016) 0504003.

[4] Y.S. Zuo, J.Y. Liu, Rigid-flexible-thermal coupling dynamic modeling a satellite-solar panels system in low earth orbit, Journal of Vibration and Shock 36(6)(2017) 38-46.

[5] H.Y. Wang, W. Zhang, Infrared characteristics of on-orbit targets based on space-based optical observation, Optics Communications 290(2013) 69-75.

[6] X.D. Wu, Influence of multilayer heat insulation material on infrared feature of a satellite, Infrared and Laser Engineering 44(6)(2015) 1721-1725.

[7] Y.J. Lu, Y.G. Han, Research on thermal characteristics of three axis stabilized satellite, Journal of Naval Aeronautical and Astronautical University 32(4)(2017) 351-357.

[8] W.T. Shen, D.Q. Zhu, L.C. Shi, G.B. Cai, Optical properties of sun synchronous orbit satellite, Journal of Beijing University of Aeronautics and Astronautics 39(1)(2013) 6-10.

[9] L. Yang, X.Y. Lv, W. Jin, J.J. Zhao, H. Yang, The model and calculation of the satellite infrared radiation periodic features, Opto-Electronic Engineering 41(2)(2014) 69-74.

[10] M.A. Gadalla, Prediction of temperature variation in a rotating spacecraft in space environment, Applied Thermal Engineering 25(14-15)(2005) 2379-2397.

[11] F.B. Li, X.J. Xu, Infrared signature simulation model for space objects, Journal of Beijing University of Aeronautics and Astronautics 35(11)(2009) 1330-1334.

[12] F.B. Li, X.J. Xu, Modeling time-evolving infrared characteristics for space object with mircromotions, IEEE Transactions on Aerospace and Electronic Systems 48(4)(2012) 3567-3577.

[13] D.Q. Zhu, W.T. Shen, G.B. Cai, W.N. Ke, Numerical simulation and experimental study of factors influencing the optical characteristics of a spatial target, Applied Thermal Engineering 50(2013) 749-762.

[14] H.X. Mao, H. Nan, J. Ma, Y.B. Dong, K.F. Wu, Analysis of influence of motion of attitude to optical character of space

target, Infrared and Laser Engineering 36(suppl.)(2007) 411-414.

[15] J.L. Liu, Y.B. Wu, H.Z. Lu, B.D. Zhao, Micromotion dynamics and geometrical shape parameters estimation of exoatmospheric infrared targets, Optical Engineering 55(11)(2016) 113103.

[16] V.C. Chen, F. Li, S.S. Ho, H. Wechsler, Micro-doppler effect in radar: phenomenon, model, and simulation study, IEEE Transactions on Aerospace and Electronic Systems 42(1)(2006) 2-21.

[17] J.P. Holman, Heat Transfer, ninth ed., McGraw-Hill, NewYork, 2005.

[18] D.R. Croft, D.G. Lilley, Heat Transfer Calculations using Finite Difference Equations. Applied Science Publishers, London, 1977.

[19] S.L. Gao, X.Y. Tang, Y. Yu, F.T. Xue, The modeling and simulation of the artificial space object, in: Proc. SPIE 7383, 2009.